KSME

Springer

Journal of Mechanical Science and Technology 35 (11) 2021

Original Article
DOI 10.1007/s12206-021-1021-2

Keywords:
· Large vertical centrifugal pump
· Hydraulic components' matching
· Hump
· Multilayer backpropagation neural network
· Particle swarm optimization

Correspondence to:
Desheng Zhang
zds@ujs.edu.cn

Citation:
Yang, G., Zhao, X., Zhang, D., Geng, L., Yang, X., Gao, X. (2021). Hydraulic components' matching optimization design and entropy production analysis in a large vertical centrifugal pump. Journal of Mechanical Science and Technology 35 (11) (2021) 5033~5048.
http://doi.org/10.1007/s12206-021-1021-2

Received April 6th, 2021
Revised July 12th, 2021
Accepted July 30th, 2021

† Recommended by Editor Yang Na

Hydraulic components' matching optimization design and entropy production analysis in a large vertical centrifugal pump

Gang Yang, Xutao Zhao, Desheng Zhang, Linlin Geng, Xueqi Yang and Xiongfa Gao

National Research Center of Pumps, Jiangsu University, Zhenjiang, Jiangsu, China

Abstract The large vertical centrifugal pump is the core power equipment for long-distance water division and large-scale irrigation projects. The power of the matching motor can reach 40 MW. In view of reducing the operating energy consumption of this kind of pump, the efficiency under the design condition was taken as the optimization objective, and a matching optimization on hydraulic components was proposed in this research. The optimization process was divided into two stages. The first stage focused on improving the configuration of the vane diffuser. In the second stage, the Plackett-Burman test design was used to screen out the optimization design variables of the vane diffuser and the volute, the optimal Latin hypercube sampling method was adopted to generate 106 sample cases, and an automatic numerical simulation optimization platform was built. Then, different approximate models were employed to construct the relationship between the optimization design variables and the objective function, and their fitting accuracy and robustness were compared. Finally, the optimal design parameters were determined by particle swarm optimization, and entropy production theory was used to analyze the internal flow pattern of the model before and after optimization. Results showed that D_3, b_4, β_3, and S_8 have the greatest impact on the hydraulic efficiency of the pump. The multilayer backpropagation neural network has a higher fitting accuracy and better robustness compared with the other three approximate models. The efficiency of the optimized model under the design condition is increased by 4.22 %, reaching 90.82 %. Reducing the number of layers and vanes of the diffuser and improving the matching of hydraulic components can dramatically improve the hydraulic performance and hump characteristics of large vertical centrifugal pumps. Entropy production theory is a reliable approach to visualizing flow loss. The turbulent flow dissipation in the vane diffuser can be reduced the most after optimization.

1. Introduction

Long-distance water diversion and large-scale irrigation projects are effective measures to solve the uneven distribution of water resources and the demand for agricultural irrigation water. The large vertical centrifugal pumps play an important role in this field owing to their large flow and high head, which also lead to larger installed power, higher energy consumption, and higher requirements for operation safety. Improving the hydraulic performance and hydraulic stability of the vertical centrifugal pumps under different operating conditions can reduce the energy consumption and improve the operational safety of pump systems.

In the past few decades, numerous works on large centrifugal pumps have been carried out by researchers. Li et al. [1] performed an unsteady simulation analysis on the hump characteristics of a pump turbine model under the pump condition. Three cascading vortex groups were observed as the pump entered the hump region. Gao et al. [2] analyzed the unsteady flow in a large centrifugal pump and investigated static performance and pressure fluctuations by using experimental data. Then, the experimental data were used to construct a more accurate numerical simulation method for large centrifugal pumps. Lu et al. [3] determined the mechanism

of the hump region on the pump performance curve from the perspective of energy balance by varying the kinetic energy of the mean flow. Most of the flow loss in a pump is transformed into turbulent flow energy, and a rotating stall with three stall cells will likely occur when operated in the hump region. Most of the existing research on large centrifugal pumps have analyzed the unstable phenomena related to the hump and stall. However, by focusing on the matching of the hydraulic components, the literature is lacking with the optimal design of hydraulic performance and stability of these pumps. The compatibility of hydraulic components of large vertical centrifugal pumps is an important issue and thus worthy of attention when discussing the process of hydraulic design.

In recent years, the application of approximate models combined with intelligent optimization algorithms has become a quick and effective optimization design method in the field of fluid machinery [4-6]. In the optimization field of rotating hydraulic components of the fluid machinery, Wang et al. [7] selected four design parameters of the pump and turbine impellers to improve system efficiency under pump and turbine conditions. The impeller was optimized using a Pareto-based genetic algorithm. Shi et al. [8] adopted a multidisciplinary optimization design for the axial flow pump impeller. The optimization goal was to ensure impeller quality and pump efficiency under the design condition. The head capacity, maximum stress value, and maximum deformation value under the part-load condition were used as constraints. Pei et al. [9] used a two-layer backpropagation neural network (BPNN) to fit the relationship between the design parameters of the centrifugal pump impeller and pump efficiency. Particle swarm optimization (PSO) was used to improve the efficiency of the centrifugal pump under the design condition.

In the optimization design of the static hydraulic components of the fluid machinery, Kim et al. [10] selected four design variables of the vane diffuser of the mixed-flow pump to optimize its design and combined the Latin hypercube sampling (LHS), radial basis neural network (RBNN), and sequential quadratic programming algorithm. Their aim was to improve the hydraulic efficiency of the mixed-flow pump under the design conditions. Pei et al. [11] used the Bezier curve to fit the shape of the elbow inlet pipe of a vertical inline pump. The shape of the elbow inlet pipe was optimized by using the artificial neural network, LHS, and multi-objective genetic algorithm under three working conditions. Wang et al. [12] used orthogonal experiments to determine the influence of four parameters of a high-power centrifugal pump diffuser on the equipment's efficiency and used the response surface model (RSM) to fit the quadratic polynomial function between the parameters and the efficiency of the centrifugal pump. The island genetic algorithm was used to solve the function and obtain the optimal parameter combination. The efficiency of their optimized centrifugal pump increased by 8.65 %.

The purpose of this research is to improve the hydraulic performance and operational stability of large vertical centrifugal pumps in a two-stage optimization design process. To achieve the objectives, this study attempts to improve the hydraulic efficiency under the design condition and optimize the self-developed large vertical centrifugal pump by combining the multilayer BPNN and PSO. In addition, an entropy production method is employed to analyze the internal flow characteristics and visualize the flow loss of the hydraulic components before and after the optimization.

2. Computation model and numerical methodology

2.1 Large vertical centrifugal pump

The computation model of the large vertical centrifugal pump in this research is developed using a similar conversion method for prototype pumps. The computational domain comprises an elbow inlet pipe, a centrifugal impeller, guide vanes, stay vanes, and a spiral volute, as shown in Fig. 1.

The similarity in conversion is based on the principle that the Strouhal number *Sr* and Euler number *Eu* of the prototype pump and model pump are equal. The *Sr* and *Eu* in the pump are defined by Eq. (1).

$$\begin{cases} Sr = \dfrac{D_2^{\,3} n}{Q} \\ Eu = \dfrac{gH}{D_2^{\,2} n^2} \end{cases} \tag{1}$$

where

D_2 : Impeller outlet diameter, m
n : Rotating speed, r/min
Q : Flow rate, m^3/h
g : Gravity factor, m/s^2
H : Pump head, m

Given the same *Sr* and *Eu* of the prototype pump and model pump, the corresponding flow rate and head conversion relationship can be obtained by Eq. (2).

$$\begin{cases} \dfrac{Q_{\mathrm{p}}}{Q_{\mathrm{m}}} = \dfrac{D_{2\mathrm{p}}^{\,3}}{D_{2\mathrm{m}}^{\,3}} \dfrac{n_{\mathrm{p}}}{n_{\mathrm{m}}} \\ \dfrac{H_{\mathrm{p}}}{H_{\mathrm{m}}} = \dfrac{D_{2\mathrm{p}}^{\,2}}{D_{2\mathrm{m}}^{\,2}} \dfrac{n_{\mathrm{p}}^{\,2}}{n_{\mathrm{m}}^{\,2}} \end{cases} \tag{2}$$

where the subscripts p and m represent the prototype pump and model pump, respectively.

The impeller is the core component for energy conversion of centrifugal pumps. The centrifugal impeller, which had been developed independently, is employed in this research. The main design parameters of the prototype pump and model pump based on the above similar transformation mechanism are shown in Table 1. The specific speed n_s is determined by Eq. (3).

Table 1. Main design parameters of the large vertical centrifugal pump.

Main design parameters		Prototype pump value	Model pump value
Rated flow rate	Q (m^3/s)	42.5	0.214
Head	H (m)	68	18
Rotational speed	n (r/min)	214.3	1150
Specific speed	n_s	215	215
Impeller inlet diameter	D_j (mm)	2802	274.1
Impeller outlet diameter	D_2 (mm)	3680	360
Impeller outlet width	b_2 (mm)	719	70.3
Blade outlet setting angle	β_2 (°)	15	15
Number of impeller blades	Z	7	7
Number of guide vanes	Z_g	20	20
Number of stay vanes	Z_s	20	20

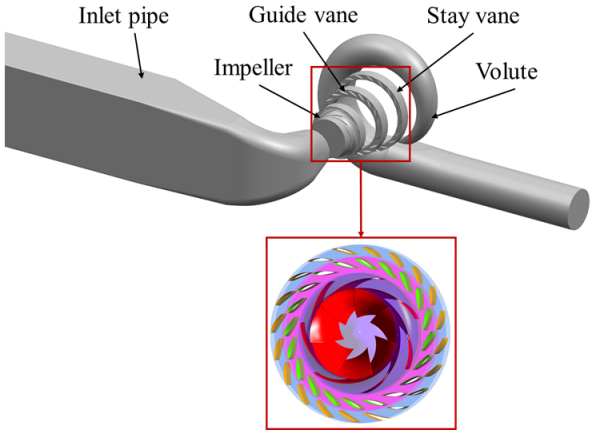

Fig. 1. Computational domain of the large vertical centrifugal pump.

$$n_s = \frac{3.65nQ^{0.5}}{H^{0.75}} \tag{3}$$

where

n_s : Specific speed

The guide vanes and stay vanes are also key hydraulic components in large hydraulic turbines or pumps, as both components play the role of controlling the flow rate and the flow pattern. The model pump described above is used as the original model for the optimization work. The details are provided in the next sections.

2.2 Grid generation

The accuracy and reliability of the numerical simulation results depend on the quality of the computational grid. The computational domain was fully discrete, and hexahedral structured grids were constructed using the ANSYS pre-processor ICEM computational fluid dynamics (CFD). Local grid refinement was applied to the near-wall regions, and y+ was less than 80, which meets the wall function requirements of the turbulence model. The grid division is shown in Fig. 2. Moreover, a grid independence test was conducted by setting seven groups of computational domain grids with different numbers. The results are shown in Fig. 3.

As shown in Fig. 3, when the number of grids is higher than 7 million, the variation in head coefficient C_H and efficiency tend to stabilize. As the calculation accuracy and computational cost need to be balanced, the total number of grids was finally determined to be 7 million, the inlet pipe grids were approximately 1.03 million, the impeller grids were approximately 1.74 million, the guide vane grids were approximately 1.55 million, the stay vane grids were approximately 820000, and the volute grids were approximately 1.86 million.

2.3 Computation setup

The commercial code ANSYS CFX was used to solve the steady 3D Reynolds-averaged Navier–Stokes (RANS) equations and predict the performance indices of the large vertical centrifugal pump. The shear-stress transport (SST) k-ω turbulence model was used in this work. The SST k-ω turbulence model can improve the definition of eddy viscosity as it considers the effect of the turbulent principal SST, thus improving the

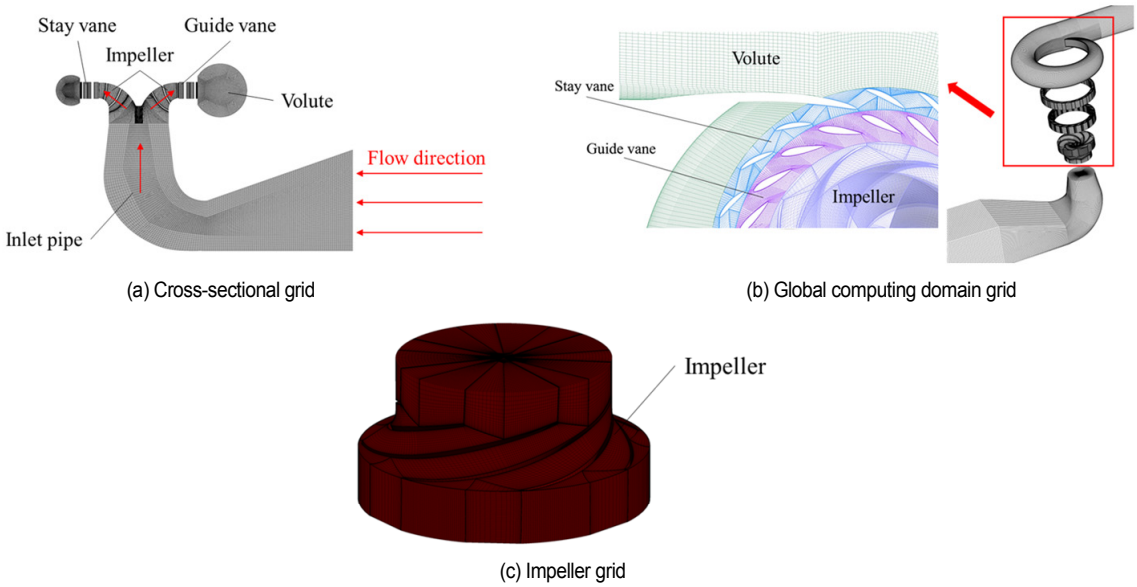

(a) Cross-sectional grid

(b) Global computing domain grid

(c) Impeller grid

Fig. 2. Grid of computational domain of the large vertical centrifugal pump.

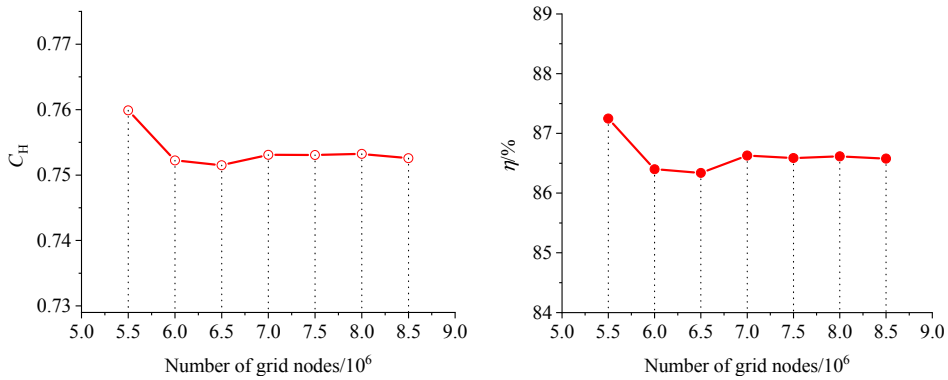

Fig. 3. Grid independence test.

prediction of the inverse pressure gradient flow [13]. The boundary conditions were set as follows. The total pressure at the inlet was 1 standard atmosphere, and the boundary conditions at the outlet were set as "mass flow rate," with a specified value of 214 kg/s. The rotating speed of the impeller was set at 1150 r/min, and the interface between the rotating domain and stationary domain was set as "frozen rotor." The solid wall meets the no-slip condition and was set as the "no-slip wall." The residual error of the convergence was defined as 10^{-5}, and the maximum number of steps was set as 1500.

2.4 Calculation results and experimental verification

The accuracy of the numerical simulation method used in this research was verified on the basis of the external characteristic test of the original model pump. The test was conducted using the national model hydraulic test bench at the BIDR of China. Fig. 4 shows the operating system of the test bench. Fig. 5 presents the physical components of the closed experiment bench and impeller of the vertical centrifugal pump. Fig. 6 illustrates the external characteristic curves of the original model pump obtained from the experiment and CFD simulation. In the figure, C_H and C_Q represent the head coefficient and flow coefficient defined by Eqs. (4) and (5), respectively. According to both equations, in this research, the flow coefficient corresponding to the design condition is 0.124, while the design head coefficient is 0.751. The trend of the head coefficient and efficiency at different flow rates as predicted by CFD are consistent with the experiment results. The maximum deviation between the calculated and tested efficiency and head values is less than 5 %, which is acceptable. The numerical simulation method used in this research has therefore been proven to be reliable.

$$\begin{cases} C_H = \dfrac{2gH}{u_2^2} \\ u_2 = \dfrac{\pi D_2 n}{60} \end{cases}, \tag{4}$$

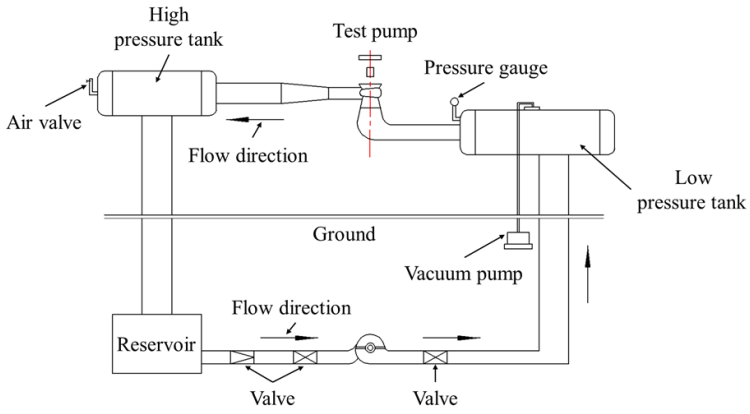

Fig. 4. System diagram of the test devices.

Fig. 5. Physical diagram of the test equipment.

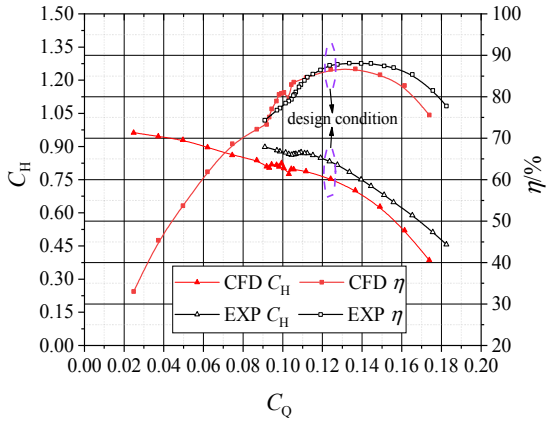

Fig. 6. Performance curves of the simulation and experiment.

$$C_Q = \frac{Q}{\pi D_2 b_2 u_2} . \quad (5)$$

3. Optimization methods and application

The process of the hydraulic components' matching optimization design for the large vertical centrifugal pump in this research is divided into two stages. The first stage focuses on improving the pump performance by changing the vane diffuser configuration. The second stage aims at optimizing the matching of the hydraulic components.

3.1 First-stage optimization and analysis

At the first stage, the vane diffuser was optimized with the purpose of improving the efficiency under the design condition of the pump. The optimization method was directed towards simplifying the guide vane and stay vane into the layer of the stay vane. After the guide vane structure was removed, the volute inlet diameter was reduced accordingly. The other arrangements were kept unchanged. The performance parameters of the single-layer stay vane model are shown in Fig. 7(a). At the same time, the blades of the stay vanes were reduced to increase the flow area between the diffuser vanes. The effects of dynamic and static interference were considered, and the number of diffuser vanes and the number of impeller blades must be mutually prime. Thus, five cases with different numbers of stay vanes were arranged. The performance parameters of each case under the design condition are also shown in Fig. 7(a). In the figure, Om represents the original model, Im represents the improved model, and the number represents the number of stay vanes. The figure shows that the single-layer stay vane model has a better performance. This finding indicates that the removal of the guide vane structure not only can simplify the model's structure but also reduce the loss of water flow in the two-layer vane diffuser. In addition, the number of stay vanes has a negligible influence on the efficiency of the model pump under the design condition, and the effect on the head was only slight. However, the energy head is comparably high when the number of stay vanes is 13. Therefore,

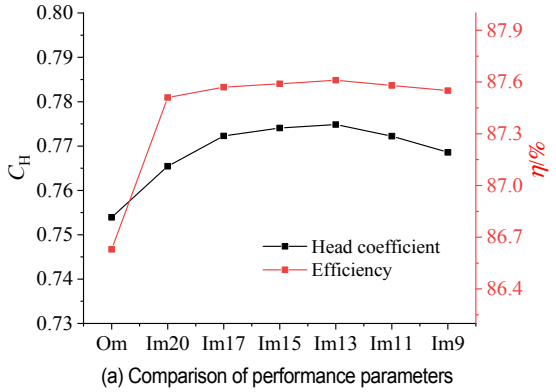

(a) Comparison of performance parameters

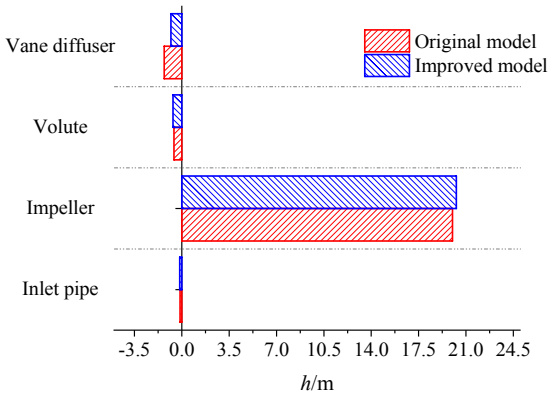

(b) Energy head distribution of the different components

Fig. 7. Performance comparison between the original model and improved model under the design condition.

after the first-stage optimization, the model with a single-layer stay vane structure and 13 stay vanes was used as the improved model. The energy head distribution comparison of each component under the design condition is shown in Fig. 7(b). The calculation method of hydraulic efficiency of the large vertical centrifugal pump is given by Eq. (6). The energy head distribution of each flow component is determined on the basis of Eq. (7).

$$\begin{cases} \eta = \dfrac{\rho g Q H}{T\omega} \\ H = \dfrac{P_{\text{tout}} - P_{\text{tin}}}{\rho g} \end{cases} \tag{6}$$

where

η : Hydraulic efficiency
T : Impeller torque, N
ω : Impeller rotation angular velocity
ρ : Fluid density, kg/m^3
P_{tout} : Total pressure at the outlet of the pump, Pa
P_{tin} : Total pressure at the inlet of the pump, Pa

$$h = \frac{P_{\text{out}} - P_{\text{in}}}{\rho g} \tag{7}$$

Table 2. Main design parameters of the diffuser and volute.

Vane diffuser and volute main design parameters		
Diffuser inlet diameter	D_3 (mm)	379.8
Diffuser outlet diameter	D_4 (mm)	434
Diffuser inlet width	b_3 (mm)	75.6
Diffuser inlet vane angle	β_3 (°)	27
Number of stay vanes	Z_s	13
Volute inlet diameter	D_5 (mm)	440
Volute inlet width	b_4 (mm)	118
Volute outlet diameter	D_6 (mm)	330

where h is the value of energy head, P_{out} is the total pressure at the outlet of the components, and P_{in} is the total pressure at the inlet of the components.

As shown in Fig. 7(b), the energy head produced by the impeller of the improved model is larger than that of the original model, the energy head loss in the vane diffuser decreases after optimization, and the energy head loss in the elbow inlet pipe and volute is nearly unchanged with respect to that of the original model. All of the findings confirm that the performance of the vane diffuser and impeller has improved. The computation domain of the improved model is obtained after the first optimization stage (Fig. 8). The basic parameters are listed in Table 2.

However, Fig. 7(b) also shows that the hydraulic loss in the vane diffuser and volute remains to be large. This finding may be attributed to the low matching of the hydraulic components. The vane diffuser is at a key position in the core hydraulic components, suggesting that its compatibility with the impeller and volute may be one of the key factors affecting the performance of large vertical centrifugal pumps. Hereafter, a second-stage optimization is conducted for the improved model.

3.2 Second-stage optimization

The second-stage optimization process is shown in Fig. 9. First, the ten design parameters of the vane diffuser and volute were selected as the initial optimization parameters. The Plackett–Burman test was conducted to determine the final optimization design variables that could greatly impact the objective function. Then, the optimal Latin hypercube sampling (OLHS) method was used to design the sample cases, and an automatic numerical simulation optimization platform was built to quickly obtain the corresponding optimization objective of the sample cases. Furthermore, multiple approximate models were used to construct the nonlinear relationship between the design variables and objective function. Finally, the optimal parameters were combined via PSO.

The large vertical centrifugal pump was subsequently redeveloped using the optimized parameters. The corresponding CFD simulation was performed to obtain the optimized hydraulic efficiency under the design condition.

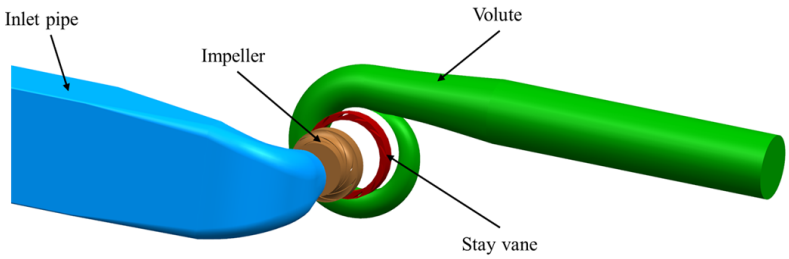

Fig. 8. Computational domain of the improved model.

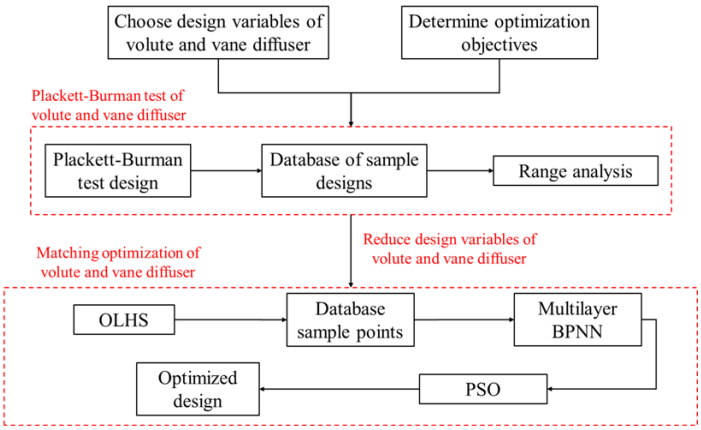

Fig. 9. Optimization procedure of the large vertical centrifugal pump.

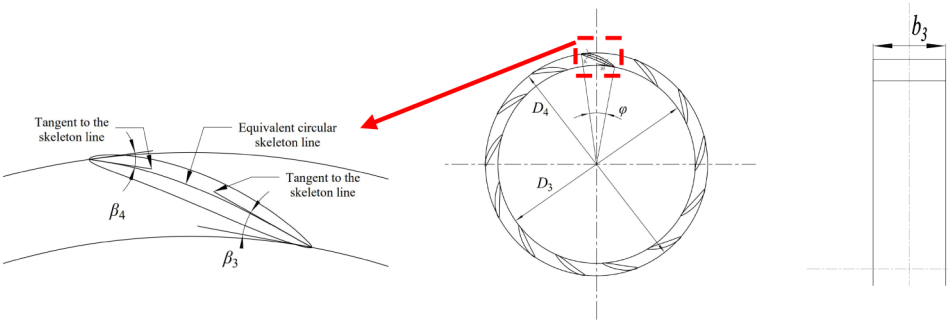

Fig. 10. The definition of the main optimization design variables of the vane diffuser.

3.2.1 Objective function

The objective function of our optimization design can be described as follows:

$$Maximum: \begin{cases} F(x) = F_1(x) \\ F_1 = \eta \end{cases} \tag{8}$$

where x represents the optimization design variables, and F_1 is the optimization objective function.

In this research, the optimization objective corresponds to the hydraulic efficiency under the design condition. Therefore, the optimization objective function should be maximized as a means of reducing the operating energy consumption.

3.2.2 Optimization design variables

The design parameters of the vane diffuser greatly affect its matching degree with the impeller and volute. Therefore, the following six main design parameters of the vane diffuser were selected as the optimization design variables: D_3, D_4, φ, β_3, β_4, and b_3. The specific design parameters are shown in Fig. 10.

As the matching characteristic between the vane diffuser and the volute needs to be considered, the following four design parameters of the volute were also selected as optimization design variables: b_4, L, D_6, and S_8. The specific design parameters are shown in Fig. 11. The eighth section in the figure is also called the volute throat, and its area equals the core parameter in the design of the volute. The area of the other cross-sections was also determined on the basis of the throat area. The velocity coefficient method is one of the commonly used methods of determining the area of the throat; this aspect is given by Eq. (9) in this research. However, the existence of empirical coefficients may lead to greater uncertainty.

Table 3. Range of different factors investigated using the Plackett–Burman test.

Variables	Factors (unit)	Parameters' name	Low level (−)	High level (+)
X_1	b_3 (mm)	Diffuser inlet width	71	90
X_2	D_3 (mm)	Diffuser inlet diameter	374	384
X_3	D_4 (mm)	Diffuser outlet diameter	426	434
X_4	β_3 (°)	Diffuser inlet vane angle	20	30
X_5	β_4 (°)	Diffuser outlet vane angle	10	20
X_6	φ (°)	Diffuser vane wrap angle	16	22
X_7	b_4 (mm)	Volute inlet width	100	130
X_8	L (mm)	Height of volute diffusion tube	600	800
X_9	D_6 (mm)	Volute outlet diameter	300	350
X_{10}	S_8 (mm^2)	Volute throat area	50000	60000
X_{11}	Virtual factor			

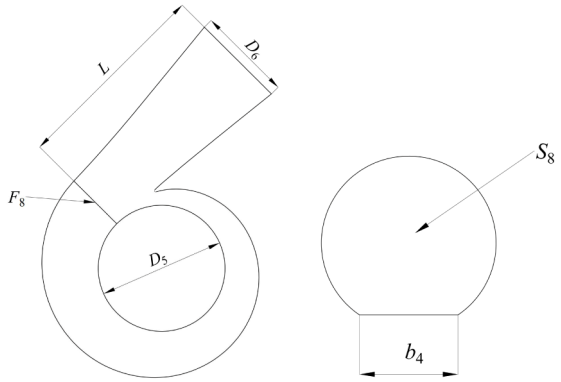

Fig. 11. The definition of the main optimization design variables of the volute.

$$\begin{cases} S_8 = \dfrac{Q}{v_3} \\ v_3 = k_3\sqrt{2gH} \\ S_\varphi = \dfrac{\varphi_0}{\varphi_8} S_8 \end{cases} \tag{9}$$

where S_8 is the volute throat area, v_3 is the average velocity of the volute section, k_3 is the speed factor, φ_0 is the angle between the section and the zero section, and S_φ is the φ section area of the volute.

3.2.3 Plackett–burman test design

A good Plackett–Burman test design [14] can efficiently screen out the factors that significantly affect the test indicators. This testing method only needs N times of calculation (i.e., N is in multiples of four) for (N-1) factors. In this research, the ten design parameters of the vane diffuser and volute in the large vertical centrifugal pump were selected, and the calculations were performed 12 times. Table 3 lists the selected parameters and the level of the test design. Table 4 presents the 12 groups of test schemes and the efficiency obtained by CFD under the design condition. On the basis of the calculation results shown in Table 4, a regression equation with efficiency as the evaluation index could be established. Table 5 shows the Pearson correlation coefficient and significance test results (one-tailed probability p-values) among the efficiency results under the design condition for the ten design parameters. The closer is the Pearson coefficient to 0, the weaker is the correlation. The closer is the p-value to 0, the greater is the correlation.

As shown in Table 5, the correlation coefficient of D_3 is 0.615, and the significance of the one-tailed test is 0.017. This finding indicates that D_3 has the greatest influence on the efficiency value, and the correlation is positive. Moreover, the correlation coefficient of S_8 to the efficiency is -0.434, and the significance of the one-tailed test is 0.079. This value represents the second largest factor affecting hydraulic efficiency, and the correlation is negative. Similarly, b_4 and β_3 have a great influence on efficiency. In summary, these four design parameters are greatly related to the efficiency of the pump.

3.2.4 OLHS

The abovementioned four parameters were eventually selected as the final optimization design variables, and OLHS was implemented on the sample data within the range of the design variables (Table 6) [15]. The 106 groups of sample points obtained within the assigned range could fully meet the number of samples required to construct a high-precision ap-

Table 4. Plackett–Burman test scheme and results.

Test number	Corresponding parameter										Optimization objective
	b_3	D_3	D_4	β_3	β_4	φ	b_4	L	D_6	S_8	η/(%)
1	90	374	434	20	10	16	130	800	350	50000	84.88
2	71	374	434	30	20	16	130	800	300	60000	85.41
3	71	384	434	20	20	16	100	600	350	60000	87.78
4	90	384	426	30	20	16	130	600	300	50000	88.23
5	90	384	426	30	10	16	100	800	350	60000	87.37
6	71	384	434	30	10	22	130	600	350	50000	89.1
7	90	374	426	20	20	22	130	600	350	60000	85.44
8	71	374	426	30	20	22	100	800	350	50000	87.58
9	90	384	434	20	20	22	100	800	300	50000	88.67
10	90	374	434	30	10	22	100	600	300	60000	86.55
11	71	384	426	20	10	22	130	800	300	60000	85.32
12	71	374	426	20	10	16	100	600	300	50000	86.53

Table 5. Regression coefficient of efficiency.

Variables	Factors (unit)	Pearson correlation	Significance (one-tailed)	Number of cases
X_1	b_3 (mm)	−0.035	0.457	12
X_2	D_3 (mm)	0.615	0.017	12
X_3	D_4 (mm)	0.117	0.358	12
X_4	β_3 (°)	0.343	0.138	12
X_5	β_4 (°)	0.205	0.261	12
X_6	φ (°)	0.150	0.321	12
X_7	b_4 (mm)	−0.372	0.117	12
X_8	L (mm)	−0.268	0.199	12
X_9	D_6 (mm)	0.088	0.393	12
X_{10}	S_8 (mm^2)	−0.434	0.079	12

Table 6. Range of optimization design variables.

Design variables	Lower	Upper	Original
D_3 (mm)	374	390	379.8
β_3 (°)	25	40	27
b_4 (mm)	100	150	118
S_8 (mm^2)	30000	60000	50650

proximate model.

3.2.5 Automatic optimization platform

The procedures of geometric modeling, grid generation, and numerical simulation of all samples were integrated by the professional optimization platform Isight [15] to improve the efficiency of data acquisition and ensure the consistency of numerical calculation accuracy of each sample. CFturbo, a turbomachinery design software, was used to realize the parametric design of the vane diffuser and volute of the large vertical centrifugal pump. The ICEM CFD, which is controlled by a script file, was employed to generate the unstructured grid of all samples under the same parameter settings. The CFX code was adopted to resolve the flow field. Subsequently, the CFturbo, ICEM CFD, and CFX were integrated using a batch processing command in Isight. With this approach, an automatic numerical simulation optimization platform for integrating the design and simulation of the large vertical centrifugal pump could be readily built. The basic process of the integrated operation is shown in Fig. 12.

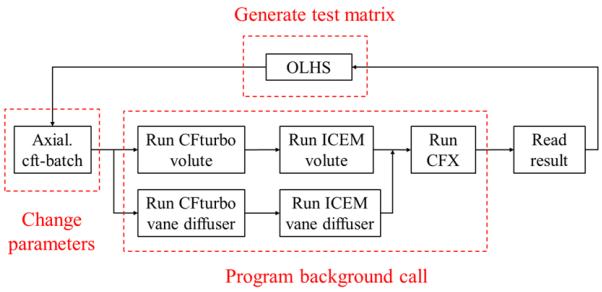

Fig. 12. Software integration framework.

3.2.6 Approximate model

An approximate model is important in constructing the rela-

tionship between the optimization parameters and optimization objectives [16, 17]. The fitting accuracy of the approximate model can greatly affect its prediction ability, and it is also one of the important factors affecting the reliability and precision of the optimization results. The approximate model can be described by Eq. (10).

$$y(x) = \tilde{y}(x) + \zeta \tag{10}$$

where $y(x)$ is the value of the actual response, $\tilde{y}(x)$ is the value of the approximate response, and ζ is a random error.

Four commonly used approximation models, namely, RSM [18], Kriging model [19], RBNN model [20], and multilayer BPNN model, were used to fit the nonlinear relationship between the optimization design variables and objective function in relation to the 106 groups of samples. In this research, 85 % of the samples were used to construct the approximate model, whereas the remaining 15 % were used to verify the approximate model. The fitting accuracy of the different approximation models was evaluated using the R^2 value, which is expressed by Eq. (11).

$$R^2 = 1 - \frac{\sum (y - \hat{y})^2}{\sum (y - \bar{y})^2} \tag{11}$$

where y is the sample point output, $\hat{y}$ is the approximate model prediction output, and $\bar{y}$ is the approximate model average output. The closer is the R^2 value to 1, the higher is the fitting accuracy of the approximate model. Each approximate model was fitted three times to ensure robustness. The comparison results of approximate models are shown in Table 7. The prediction accuracies of the RSM and Kriging models were lower than the neural network model, suggesting prediction instability. The prediction accuracy of the RBNN model was high, but the multilayer BPNN performed better in terms of prediction accuracy and prediction stability. Therefore, the multilayer BPNN was selected as the final approximate model in the optimization process. The network structure of the multilayer BPNN is shown in Fig. 13. The model has a strong ability to fit the nonlinear function relationship, which is divided into the input layer, hidden layers, and output layer. The multilayer BPNN is beneficial to use because it contains multiple hidden layers that can adapt to stronger nonlinear functional relationships. The multilayer BPNN used in this research contains three hidden layers, and the corresponding number of neurons is 4, 8, and 2. This network is used to fit the relationship between the four design variables and the objective function.

3.2.7 PSO

The PSO, which was first proposed by Kennedy and Eberhart in 1995 [21, 22], is an intelligent global optimization algorithm. The basic idea of PSO is inspired by the way birds and fish search for food in nature. PSO has become one of the

Table 7. Analysis of the R^2 value of the different approximate models.

Approximation model	First R^2	Second R^2	Third R^2
RSM	0.9224	0.9646	0.9573
Kriging model	0.9437	0.8809	0.8734
RBNN model	0.9934	0.9881	0.9858
Multilayer BPNN model	0.9921	0.9976	0.9995

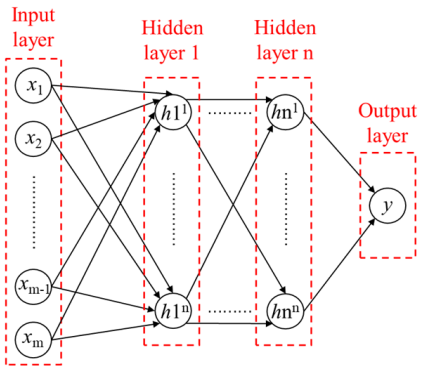

Fig. 13. Multilayer BPNN structure.

preferred algorithms among the many optimization algorithms because of its high convergence efficiency. In each iteration, a particle in the PSO updates its position by using two "extreme value" positions. The first one is the optimal solution obtained by the particle itself called the individual extreme value. Then, another "extreme value" representing the optimal solution is found by the whole population, and it is called the global extreme value. The update speed and update location of the particles can be expressed as Eqs. (12) and (13), respectively.

$$v_{id} = \omega_1 v_{id} + c_1 r_1 (p_{id} - x_{id}) + c_2 r_2 (p_{gd} - x_{id}), \tag{12}$$

$$x_{id} = x_{id} + v_{id} \tag{13}$$

where ω_1 is the inertia factor (the larger is the value, the stronger is the global optimization ability); p_{id} represents the d-dimensional individual extreme value of the i-*th* variable; p_{gd} represents the d dimension of the global optimal solution; c_1 and c_2 are constants and usually set to 2; and r_1 and r_2 are random numbers in the interval of [0, 1].

The PSO algorithm in this research was combined with the trained multilayer BPNN to solve the optimization problem of the large vertical centrifugal pump. Table 8 shows the parameter setting of the PSO.

4. Results and analysis

4.1 Comparison of external characteristics before and after optimization

The PSO was adopted in this work to search the global opti-

Table 8. Parameter setting of PSO.

Parameter setting	Value
Maximum iterations	100
Number of particles	24
Inertia	0.9
Global increment	0.8
Particle increment	0.9
Maximum velocity	0.1
Maximum convergence iterations	5
Failed run penalty value	10^{-4}
Failed run objective value	10^{-4}

Table 9. Comparison of parameters between the improved model and optimized model.

Design parameters	D_3 (mm)	β_3 (°)	b_4 (mm)	S_8 (mm^2)	η (%)	H (m)
Improved model	379.8	27	118	50650	87.6	18.07
Optimized model	389.6	30.2	131.6	41896	90.82	19.11

mization of the BPNN model, and the optimal combination of the four optimization parameters was set to be within the set number of the iteration steps. Subsequently, the optimized parameters were used to reshape the geometric model and execute the CFD. A comparison of the design parameters and the performance indices between the improved model and the optimized model are given in Table 9. Under the design condition, the hydraulic efficiency of the optimized model can reach 90.82 %, while the head can reach 19.11 m. The efficiency of the optimized model under the design condition is 3.22 %, a value higher than that of the improved model and 4.22 % higher than that of the original model. Additionally, the optimal efficiency predicted by the multilayer BPNN model is 90.59 %, which is only 0.23 % different from the actual value given by the numerical simulation, further depicting the reliability and accuracy of the multilayer BPNN model.

In view of further analyzing the changes in the performance of the optimized model under multiple operating conditions, the external characteristics curves of the optimized model, improved model, and original model are compared (Fig. 14). The efficiency and head of the optimized model under multiple conditions are significantly higher than those of the improved and original models, except for the overload region where the improved model has a better performance than the optimized model. In addition, as shown in Fig. 14(b), the positive slope of the *Q-H* curve (hump characteristic) of the original model is significantly enhanced for the improved and optimized models. The positive slope trend of the optimized model's hump curve has dramatically decreased, and the hump region is farther away from the design condition. We can therefore conclude that the hump characteristic of large vertical centrifugal pumps

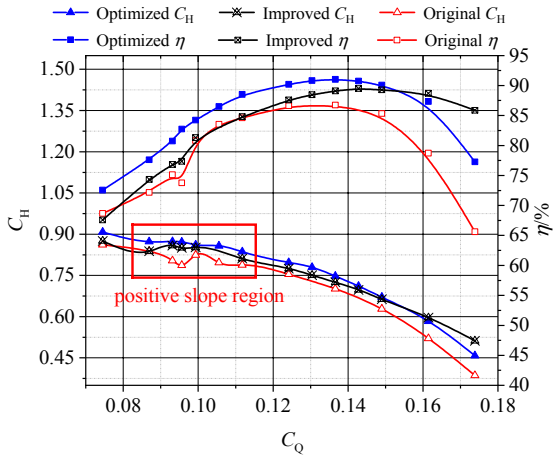

(a) External characteristic curve

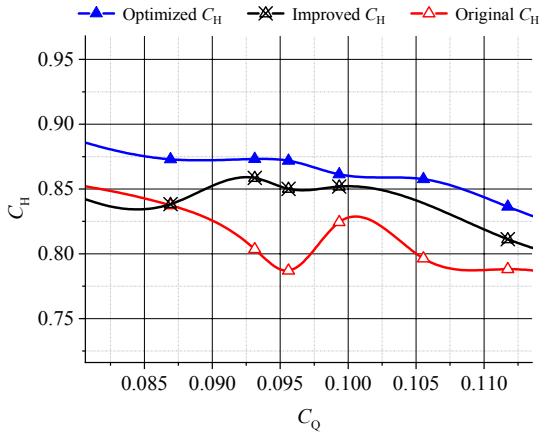

(b) Hump characteristic curve

Fig. 14. Comparison of pump performance of original model, improved model and optimized model.

can be improved by optimizing two important factors, namely, the number of layers and vanes of the diffuser, and the appropriate matching of the hydraulic components.

4.2 Flow analysis

4.2.1 Entropy production theory

Entropy production theory [23, 24] was adopted in this work to further analyze the internal flow characteristics and visualize the flow loss of the hydraulic components before and after optimization. As the internal flow of a large vertical centrifugal pump is an irreversible process, the energy dissipation caused by the flow loss inevitably leads to an increase in entropy. The numerical simulation of large vertical centrifugal pumps is generally considered to be an incompressible flow. The entropy production caused by the heat transfer can thus be ignored by approximation, and the entropy production in the hydraulic components is instead considered to be mainly caused by the turbulent flow dissipation. The two constituent parts are given by Eq. (14): the direct dissipation entropy production rate

(EPR) of $S_{PRO,\bar{D}}$ and the turbulent dissipation EPR of $S_{PRO,D'}$.

The direct dissipative EPR of $S_{PRO,\bar{D}}$ can be calculated using Eq. (15). However, the turbulent dissipative EPR of $S_{PRO,D'}$ cannot be directly solved by the RANS method via CFD calculation. Previously, Kock and Herwig [25] proposed an alternative calculation method based on the turbulence model, which is given by Eq. (16).

Entropy production theory was used in this research to compare the internal flow loss between the improved model and optimized model. The magnitude of EPR can usually represent the flow loss in the hydraulic components. Assume that the temperature of the internal flow field of the large vertical centrifugal pump is constant. Then, the EPR can be defined as Eq. (17).

$$\frac{\overline{\Phi}}{T} = S_{PRO,\bar{D}} + S_{PRO,D'}, \tag{14}$$

$$S_{PRO,\bar{D}} = \frac{\mu}{\overline{T}}\left\{2\left[\left(\frac{\partial \bar{u}}{\partial x}\right)^2 + \left(\frac{\partial \bar{v}}{\partial y}\right)^2 + \left(\frac{\partial \bar{w}}{\partial z}\right)^2\right] + \left(\frac{\partial \bar{u}}{\partial y} + \frac{\partial \bar{v}}{\partial x}\right)^2 + \left(\frac{\partial \bar{u}}{\partial z} + \frac{\partial \bar{w}}{\partial x}\right)^2 + \left(\frac{\partial \bar{v}}{\partial z} + \frac{\partial \bar{w}}{\partial y}\right)^2\right\} \tag{15}$$

where μ is the hydrodynamic viscosity, and u, v, and w represent the components of the velocity in the x, y, and z axial directions, respectively.

$$S_{PRO,D'} = \frac{\rho\varepsilon}{\overline{T}} \tag{16}$$

where ε is the turbulence dissipation rate, and $\overline{T}$ is the temperature.

$$\Phi = \overline{T} \times S_{PRO,D'} + \overline{T} \times S_{PRO,\bar{D}}. \tag{17}$$

4.2.2 Entropy production analysis in vane diffuser

Fig. 15 shows a comparison of the EPRs in the vane diffuser, volute, and impeller before and after optimization under the design condition. Among the hydraulic components of the original model, the EPR in the vane diffuser is the highest, followed by that of the impeller, whereas the smallest that in the volute. The vane diffuser is close to the impeller, and a poor design can easily lead to large internal flow losses. As the main energy conversion component, the impeller has a complex internal flow and is prone to high flow loss, whereas the flow loss in the volute is generally small. After optimization, the EPR in the impeller remains almost unchanged, and the EPR in the vane diffuser is clearly decreased. The EPR in the volute is also slightly reduced, indicating that the efficiency improvement of the optimized model under the design condition is mainly caused by the reduction of turbulent flow dissipation in the vane diffuser. The vane diffuser is in the middle position of

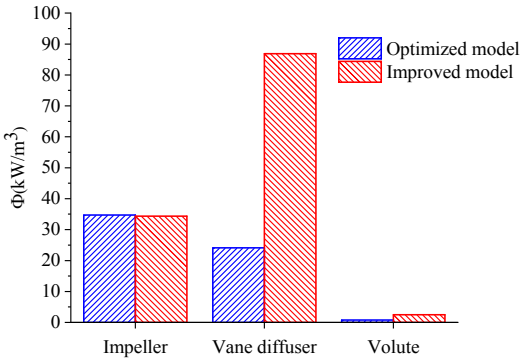

Fig. 15. Comparison of EPR at design condition for each component.

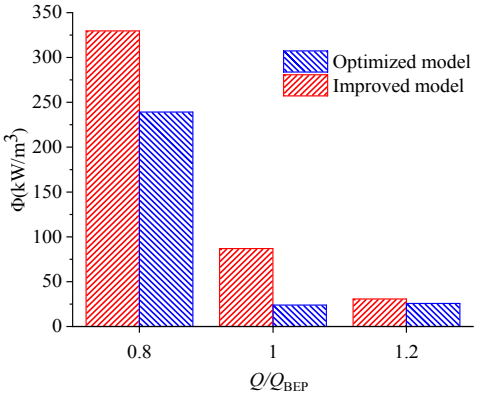

Fig. 16. Comparison of EPRs at different conditions for vane diffuser.

the hydraulic components, and the turbulent flow dissipation in the vane diffuser is significantly reduced. This condition indicates that the matching between the vane diffuser and impeller is enhanced after the optimization.

The EPRs in the vane diffuser with different flow rates are compared (Fig. 16). The comparison was conducted to further analyze the influence of turbulence dissipation in the vane diffuser on the large vertical centrifugal pump under the different operating conditions before and after optimization. The EPR in the vane diffuser of the optimized model is lower than that of the improved model for all three conditions. The lowest EPR in the vane diffuser of the improved model appears under the overload condition, while the optimized model has the lowest EPR in the vane diffuser under the design condition. The decrease in EPR in the vane diffuser is most obvious under the part-load condition, while the decrease is smaller under the overload condition. Hence, the optimized vane diffuser is more compatible with the impeller under multiple operating conditions, and the matching of the vane diffuser and impeller has a more significant impact on the hydraulic performance under the part-load condition.

Three different spans in the vane diffuser are selected for the visualization of the EPR distribution, as shown in Fig. 17. Fig. 18 shows the corresponding contours of the EPR distribution under the design condition. The tendency is similar between the improved and optimized models. In particular, the EPR is

the largest at the 0.2 span, whereas the lowest is at the 0.8 span. However, the improved model has a significantly higher EPR for all three vane diffuser spans, while the optimized model simply gives a much smaller EPR. In addition, for the optimized model, the EPR at the vaneless region and the leading edge of the vane diffuser is largely reduced, and the EPR distribution in the circumferential direction of each span is more uniform. However, some regions have a high EPR at the trailing edge of the vane diffuser.

The axial flow in the vane diffuser may be regarded as the main reason for the uneven distribution of EPR among the different spans. The increasement of inlet diameter of the optimized vane diffuser enlarges the range of the vaneless region between the vane diffuser and the impeller, thus weakening the mutual interference between the impeller and vane diffuser. The increase in the diffuser inlet angle implies improved compatibility with the incoming flow. A more even distribution of EPR in the circumferential direction is indicative of the improved matching of the vane diffuser and impeller. Part of the high EPR regions at the trailing edge of the vane diffuser may have been caused by the flow separation.

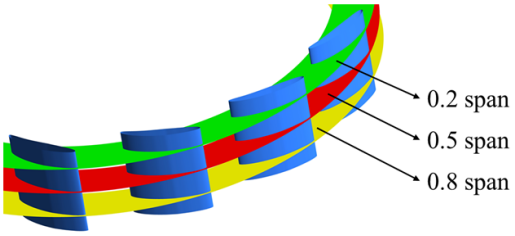

Fig. 17. Schematic diagram at different spans of the vane diffuser.

4.2.3 Flow pattern analysis in vane diffuser and volute

Fig. 19 shows the EPR distribution in the vane diffuser and volute under the design condition. As shown in Fig. 19(a), in the improved model, the high EPR regions extend to the volute inlet from the vane diffuser, and the EPR is unevenly distributed in the circumferential direction. The EPR on the side with the larger cross-sectional area of the volute is higher than that on the side with the smaller cross-sectional area. The EPR shows a higher level in the volute tongue and the corresponding diffuser vane flow channel. The band-shaped regions with high EPR appear in the volute, indicating the great influence of the flow characteristics in the vane diffuser on the volute. By contrast, as shown in Fig. 19(b), the high EPR regions of the optimized model in the volute are significantly reduced, and the distribution is more uniform. Although some high EPR regions still exist in the trailing edge of the diffuser vane, the flow in the volute domain is not likely to be affected significantly. Compared with Fig. 19(a), the magnitude of EPR in the volute tongue and the corresponding diffuser vane channel is greatly reduced. The optimized volute decreases the cross-sectional area and increases the inlet width, which leads to a more reasonable matching between the vane diffuser and volute. Consequently, the optimized volute has an enhanced diversion effect on the outlet flow of the vane diffuser, and this scenario can more efficiently convert kinetic energy into pressure energy.

Fig. 20 shows the velocity and streamline distribution in the vane diffuser and volute under the design condition. As shown in Fig. 20(a), low-velocity regions and high-velocity regions alternately appear in the diffuser vane channel of the improved model. The high-velocity regions mostly appear on the side of the diffuser vane's working surface and extend from the vane-

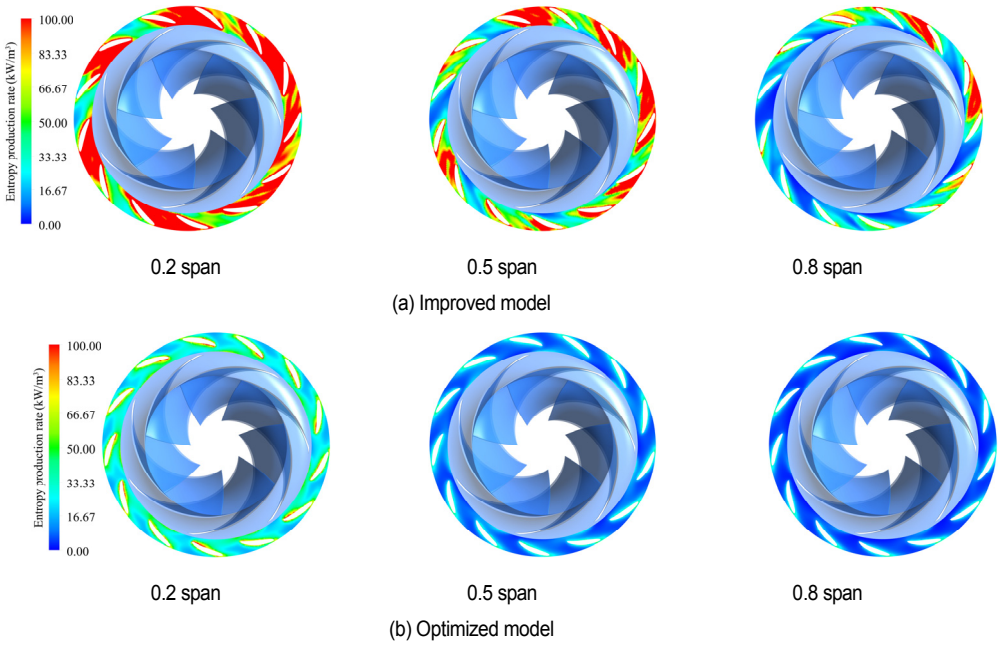

Fig. 18. EPR of vane diffuser at different spans.

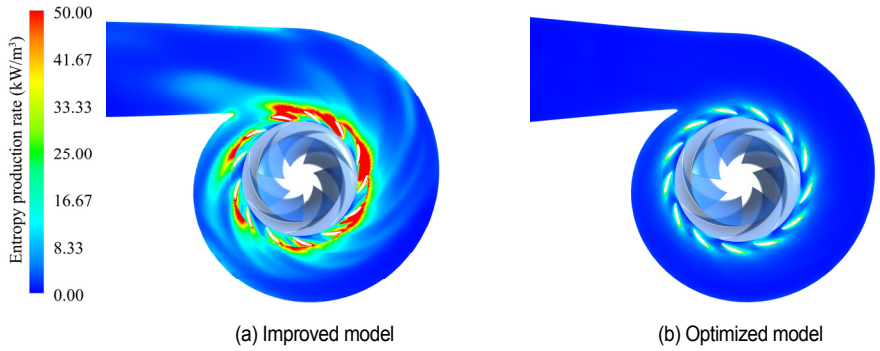

Fig. 19. Entropy production distribution of the vane diffuser and volute.

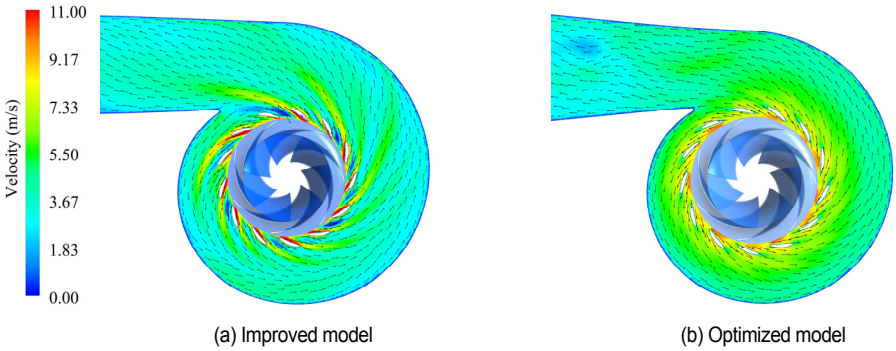

Fig. 20. Velocity and streamline distribution of the vane diffuser and volute.

less region to the volute channel. The band-shaped high-velocity zone in the volute is the reason for the high EPR. The streamlines in the low-velocity regions are more chaotic and appear more frequently on the side with a larger cross-sectional area of the volute. The low-velocity regions can potentially generate vortices, which further contribute to flow loss. The high-velocity regions on the diffuser vane's working surface are likely to produce greater impact losses. These two losses are expected to cause a higher level of EPR. The distribution of velocity and streamline shown in Fig. 20 agrees well with the EPR distribution shown in Fig. 19. The similarity indicates that using entropy production theory is a reliable approach in visualizing the flow loss.

As shown in Fig. 20(b), the low-velocity regions in the vane diffuser generally disappear after optimization, and the velocity distribution in the vane diffuser and volute is more uniform. Although part of the high-velocity regions still exists in the vaneless region, they do not extend to the diffuser vane channel. The streamlines in the optimized vane diffuser and the volute appear smoother, and no obvious vortex regions are observed. The improved matching level between the optimized vane diffuser and volute is an important reason for the improved flow pattern. Owing to the mutual interference between the impeller and vane diffuser, a part of the high-velocity regions inevitably exists in the vaneless region.

After analyzing the internal flow field of each hydraulic component via entropy production theory, we find that the matching degrees among the hydraulic components are greatly improved after optimization. The flow patterns in the vane diffuser and volute are considerably improved, resulting in a significant reduction in turbulent flow dissipation. Consequently, the overall hydraulic performance of the large vertical centrifugal pump in this research is improved.

5. Conclusions

The performance of the large vertical centrifugal pump independently developed in this research was improved by two-stage optimization. Entropy production theory was used to compare the internal flow field of the pump before and after optimization. The following conclusions are obtained:

1) The vane diffuser is an important hydraulic component in the large vertical centrifugal pump. Reducing the number of layers and vanes of the diffuser can effectively improve the hydraulic performance and hump characteristics of the pump.

2) Plackett–Burman test was employed to screen out the important design variables. Four variables (diffuser inlet diameter D_3, volute inlet width b_4, diffuser inlet vane angle β_3, and volute throat area S_8) considerably affected the hydraulic efficiency of the large vertical centrifugal pump.

3) Four approximate models, namely, the RSM, Kriging, RBNN, and BPNN models, were used to fit the relationship between the design variables and the performance parameters. The results showed that the multilayer BPNN is more effective than the other models in predicting the performance of the large vertical centrifugal pump.

4) PSO combined with multilayer BPNN was used to optimize the matching of the hydraulic components. The performance of the optimized model was better under multiple operating conditions compared with those of the two other models. The hydraulic efficiency of the optimized model under the design condition increased by 4.22 % to 90.82 %.

5) Entropy production theory can be used to visualize the flow loss inside a large vertical centrifugal pump. The EPR in the vane diffuser and volute is significantly reduced after optimization. The matching of the hydraulic components is one of the important factors affecting the hydraulic performance and hump characteristics of the large vertical centrifugal pump.

Acknowledgments

This work was financially supported by the National Natural Science Foundation of China (Grant No. 51979125), Primary Research and Development Plan of Jiangsu Province (Grant No. BE2019089), and Graduate Research and Innovation Projects of Jiangsu Province (Grant No. SJCX21_1682). The research was assisted by the Hang Zhou Jiang He Hydro-Electric Science and Technology Co., Ltd.

Nomenclature

Sr	: Strouhal number
Eu	: Euler number
n_s	: Specific speed
n	: Rotating speed, r/min
Q	: Flow rate, m^3/h
H	: Pump head, m
C_H	: Head coefficient
C_Q	: Flow rate coefficient
D_2	: Impeller outlet diameter
g	: Gravity factor, m/s^2
b_2	: Impeller outlet width, mm
η	: Hydraulic efficiency
T	: Impeller torque, N
ω	: Impeller rotation angular velocity
ρ	: Fluid density, kg/m^3
P_{tout}	: Total pressure at outlet of the pump, Pa
P_{tin}	: Total pressure at inlet of the pump, Pa
h	: Energy head value, m
P_{out}	: Total pressure at outlet of the components, Pa
P_{in}	: Total pressure at inlet of the components, Pa
x	: Optimization design variables
F_1	: Optimization objective function
S_8	: Volute throat area, mm^2
v_3	: Average velocity of volute section, m/s
k_3	: Speed factor
φ_0	: The angle between the section and the 0 section, °
S_φ	: The φ section area of the volute, mm^2
R^2	: Decisive factor
ε	: Turbulence dissipation rate
T	: Temperature

References

[1] D. Y. Li et al., Unsteady simulation and analysis for hump characteristics of a pump turbine model, *Renewable Energy*, 77 (2005) 32-42.

[2] Z. X. Gao et al., Numerical and experimental study of unsteady flow in a large centrifugal pump with stay vanes, *Journal of Fluids Engineering*, 136 (7) (2014) 071101.

[3] G. C. Lu et al., Energy balance and local unsteady loss analysis of flows in a low specific speed model pump-turbine in the positive slope region on the pump performance curve, *Energies*, 12 (22) (2019) 1829.

[4] W. J. Deng et al., An optimization method based on design of experiments and its application to centrifugal pumps, *Journal of Northwestern Polytechnical University*, 26 (6) (2008) 707-711.

[5] X. C. Gan et al., Multi-component optimization of a vertical inline pump based on multi-objective pso and artificial neural network, *Journal of Mechanical Science and Technology*, 34 (12) (2020) 4883-4896.

[6] S. Derakhshan et al., Numerical shape optimization of a centrifugal pump impeller using artificial bee colony algorithm, *Computers and Fluids*, 81 (2013) 145-151.

[7] L. Wang et al., Geometrical optimization of pump-as-turbine (PAT) impellers for enhancing energy efficiency with 1-D theory, *Energies*, 13 (16) (2020) 4120.

[8] L. Shi et al., Multi-disciplinary optimization design of axial-flow pump impellers based on the approximation model, *Energies*, 13 (4) (2020) 779.

[9] J. Pei et al., Multiparameter optimization for the nonlinear performance improvement of centrifugal pumps using a multilayer neural network, *Journal of Mechanical Science and Technology*, 33 (6) (2019) 2681-2691.

[10] J. H. Kim and K. Y. Kim, Analysis and optimization of a vaned diffuser in a mixed flow pump to improve hydrodynamic performance, *Journal of Fluids Engineering*, 134 (7) (2012) 071104.

[11] J. Pei et al., Multi-objective shape optimization on the inlet pipe of a vertical inline pump, *Journal of Fluids Engineering*, 141 (6) (2019) 061108.

[12] W. J. Wang et al., Optimization of the diffuser in a centrifugal pump by combining response surface method with multi-island genetic algorithm, *Proceedings of the Institution of Mechanical Engineers, Part E: Journal of Process Mechanical Engineering*, 231 (2) (2017) 191-201.

[13] F. J. Wang, *Computational Fluid Dynamics Analysis*, Tsinghua University Press, Beijing, China (2004).

[14] Z. W. Wang, *SPSS Statistical Analysis and Comprehensive Application*, Shanghai Jiao Tong University Press, Shanghai, China (2012).

[15] Y. Y. Lai, *Isight Theory of Parametric Optimization*, Beijing University of Aeronautics and Astronautics Press, Beijing, China (2012).

[16] D. Han and J. R. Zhang, A survey of metamodel-ling techniques in engineering optimization, *Journal of East China University of Science and Technology (Natural Science Edition)*,

38 (6) (2012) 762-768 (in Chinese).
[17] K. Wang et al., Load-balanced and locality-aware scheduling for data-intensive workloads at extreme scales, *Concurrency Computation Practice Experience*, 28 (1) (2016) 70-94.
[18] M. A. Bezerra et al., Response surface methodology (RSM) as a tool for optimization in analytical chemistry, *Talanta*, 76 (5) (2008) 965-977.
[19] J. P. C. Kleijnen, Kriging metamodeling in simulation: a review, *European Journal of Operational Research*, 192 (3) (2009) 707-716.
[20] M. W. Heo et al., High-efficiency design optimization of a centrifugal pump, *J. Mechan. Sci. Technol*., 30 (2016) 3917-3927.
[21] J. Kennedy and R. C. Eberhart, Particle swarm optimization, *Proceedings of IEEE International Conference on Neural Networks. IV* (1995) 1942-1948.
[22] Y. Shi and R. C. Eberhart, A modified particle swarm optimizer, *Proceedings of IEEE International Conference on Evolutionary Computation* (1998) 69-73.
[23] K. Bejan, *Entropy Generation through Heat and Fluid Flow*, John Wiley and Sons, Inc., New York, USA (1982).
[24] Y. D. Gu et al., Clocking effect of vaned diffuser on hydraulic performance of high-power pump by using the numerical flow loss visualization method, *Energy*, 170 (2019) 986-997.
[25] F. Kock and H. Herwig, Entropy production calculation for turbulent shear flows and their implementation in CFD codes, *International Journal of Heat and Fluid Flow*, 26 (4) (2005) 672-680.

Gang Yang is currently a Master candidate in National Research Center of Pumps, Jiangsu University. His research interests include optimization design, computational flow dynamics, and hydraulic stability of large centrifugal pumps.

Xutao Zhao is currently a Ph.D. candidate in National Research Center of Pumps, Jiangsu University. He received his M.A. degree from Lanzhou University of Technology in 2020. His research interests include the optimization design of centrifugal pumps and the internal flow investigation of axial waterjet pumps.

Desheng Zhang is currently a Professor in the National Research Center of Pumps, Jiangsu University. He received his Ph.D. from Jiangsu University in 2010. His research interests include unsteady cavitating turbulent flows in hydrofoils and pumps and the theory and optimized design of fluid machinery.